Drag reduction through self-similar bending of a flexible body

Silas Alben[*], **Michael Shelley**[*] **& Jun Zhang**[*][†]

* *Applied Mathematics Laboratory, Courant Institute of Mathematical Sciences, New York University, New York City, New York 10012, USA*
† *Department of Physics, New York University, New York City, New York 10003, USA*

The classical theory of high-speed flow[1] predicts that a moving rigid object experiences a drag proportional to the square of its speed. However, this reasoning does not apply if the object in the flow is flexible, because its shape then becomes a function of its speed—for example, the rolling up of broad tree leaves in a stiff wind[2]. The reconfiguration of bodies by fluid forces is common in nature, and can result in a substantial drag reduction that is beneficial for many organisms[3,4]. Experimental studies of such flow–structure interactions[5] generally lack a theoretical interpretation that unifies the body and flow mechanics. Here we use a flexible fibre immersed in a flowing soap film to measure the drag reduction that arises from bending of the fibre by the flow. Using a model that couples hydrodynamics to bending, we predict a reduced drag growth compared to the classical theory. The fibre undergoes a bending transition, producing shapes that are self-similar; for such configurations, the drag scales with the length of self-similarity, rather than the fibre profile width. These predictions are supported by our experimental data.

Experiments that cleanly reveal the nature of interactions between deformable bodies and flows are difficult to perform. Complications include controlling three-dimensional flow effects and visualizing the flows. Soap film is a convenient experimental system described by two-dimensional hydrodynamics in many aspects[6–10]. Our soap-film flow tunnel is illustrated in Fig. 1. Driven by gravity, soapy water (1.5% Dawn dish detergent; density $\rho = 1\,\mathrm{gm\,cm^{-3}}$) leaves an elevated reservoir and spreads into a vertical soap film (thickness $f = 1–3\,\mu\mathrm{m}$) descending between two straight nylon lines (tunnel width, 9.0 cm). Adjusting reservoir efflux rate adjusts flow velocity U through the range 0.5–3.0 m s^{-1}; breakage occurs at velocities outside this range.

Half-way down the tunnel, a thin, flexible glass fibre (length $L = 1–5$ cm; diameter, $34\,\mu\mathrm{m}$; rigidity $E = 2.8$ erg cm), glued at its midpoint to a thin rod, is inserted transverse to the flow. We measure the drag force on the fibre, record its shape, and visualize the flow structures using interferometry, all as a function of flow speed. For comparison, a much more rigid fibre is also used ($L = 2.0$ cm; $E = 2,000$ erg cm). On the basis of fibre lengths, flow velocities, and soap film viscosity ν, the Reynolds number Re $= LU/\nu$ is typically large, in the range 2,000–40,000.

Figure 2a and b shows the flow patterns around a flexible fibre at two different flow speeds. Typical of high-Reynolds-number flows past bluff bodies, they are characterized by a thin separated boundary layer which divides the wake—containing slow-moving (a few cm s^{-1}), turbulent flow in which vorticity and viscosity are important—from the rest of the flow field, which is fast and laminar. But unlike rigid-body flows, as the flow speed is increased the body changes its shape by bending and so presents a smaller profile to the flow. Figure 3a shows in alternating colour the successively more-streamlined fibre shapes as flow speed is increased. We expect this to lead to a reduced growth of drag with flow speed, and this is borne out by Fig. 4a, which compares the drag induced by a nearly rigid fibre, well-approximated by U^2 growth, with that for a flexible fibre, which shows a much decreased, more slowly growing drag. An upper bound for the contribution of skin friction to the drag can be estimated by the expression for viscous drag per unit width on a flat plate aligned with the flow[1], $1.33\rho U^2 L \mathrm{Re}^{-1/2}$. For the parameters of our experiment, this value is at least an order of magnitude below the total drag; hence form drag predominates.

As we shall argue, a natural non-dimensional control parameter that scales linearly with flow velocity is:

$$\eta = \left(\frac{\rho f L^2 U^2 / 2}{E/L}\right)^{1/2} = (L/L_0)^{3/2} \quad \text{with } L_0 = (2E/\rho f U^2)^{1/3} \quad (1)$$

Here, η involves a ratio of fluid kinetic energy to elastic potential energy, or the ratio of fibre length to an intrinsic 'bending length' L_0, which captures the competition between fibre rigidity and fluid forcing. Loaded elastic bodies often involve intrinsic length scales, such as the 'buckling length' of a beam under compression[11]. To study the scaling of drag with flow speed, we introduce the drag coefficient $C_D = \mathrm{Drag}/(\rho U^2 L f/2)$, which for a rigid object in inviscid flow depends only on its geometric shape[1]. A non-dimensional drag is defined as $D = C_D \eta^2$ so that D scales with η as the drag scales with velocity. Figure 4b plots D versus η. The data for a nearly rigid fibre (green) show approximately η^2 growth. The other data sets are for flexible fibres of equal rigidity but different lengths. The data for the longest fibre (blue) deviate at lower flow velocities, probably induced by proximity to the channel walls, but as the fibre profile narrows with increasing η, the data sets overlap. It appears that there is a transition at $\eta \approx \mathrm{O}(1)$ from η^2 scaling of drag to a new, more slowly growing form.

To interpret the experiment, we abstract its crucial features and build a mathematical model coupling hydrodynamics to body flexibility. The fibre is modelled as a thin, inextensible elastic beam loaded by the difference in fluid pressure p between its upstream and downstream sides. The pressure is found by constructing exact, steady solutions to the inviscid, incompressible Euler equations, using free-streamline theory[12] (FST). This method, based upon conformal mapping, originated[13] as a way to model flows around flat plates with a downstream wake. It has since been extended as a numerical method to compute flows around curved shapes, and to determine the shapes of sails under constant
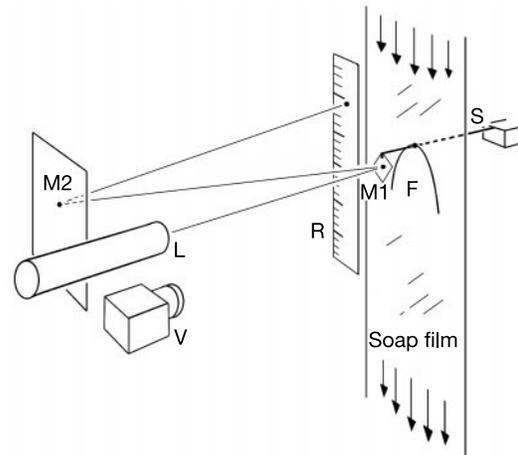

Figure 1 The layout of the experiment. A glass fibre (F) is inserted into a flowing soap-film tunnel (partly shown). The fibre is supported by a thin stainless-steel rod (S), which is clamped at one end. Fluid drag force acting on the fibre deflects this support slightly downwards. After a calibration using a known force, the drag force is determined by measuring the displacement of a laser beam (L) reflected from a small mirror (M1) mounted on S and then from a fixed mirror (M2). The rigidity of the support and the distances between the mirrors and the ruler (R) determine the overall sensitivity of the measurement. A video camera (V) records the position of the laser beam, which gives the force measurement. The soap solution is seeded with TiO$_2$ particles, allowing the flow speed to be measured by a laser Doppler velocimeter (not shown), aimed at the midline 7 cm above the filament. (Objects and distances are not drawn to scale).
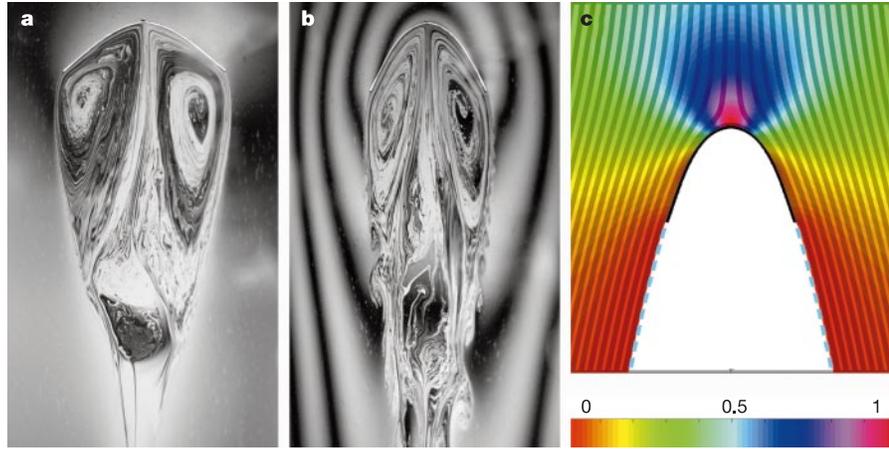
479

Figure 2 Examples of the flow field and fibre shape in experiment and model. **a,b,** Flow around a flexible fibre of length 4.1 cm and rigidity 2.8 erg cm, at flow speeds of 69 cm s^{-1} (**a**) and 144 cm s^{-1} (**b**). Monochromatic light from a low-pressure sodium lamp reflects from the two surfaces of the film, creating an interference pattern which shows small variations in film thickness. **c,** Free-streamline model solution for non-dimensional velocity $\eta = 27$. The pressure field, shown in colour, varies from its maximum value of 1 at the stagnation point on the fibre (black) to its minimum value of 0 on the free streamlines (dashed lines); overlaid are the streamlines of the flow.

tension[14]. The extension here is to simultaneously determine the body and flow as a balance of elastic forces with pressure forces. By assuming incompressibility, we neglect possible effects of flow compressibility due to thickness variations in the soap film. Preliminary studies of such effects indicate that compressibility is not a dominant influence on the flow[15,16]. In our case, this assumption seems to give a good account of the data.

The wake is represented by a stagnant region of constant-pressure fluid behind the body. Outside the wake, the flow is steady, inviscid and irrotational. 'Free streamlines' separate from the fibre ends, dividing these two regions. The main flow is a potential flow, with the boundary conditions $\mathbf{u}\cdot\mathbf{n} = 0$ on the fibre, and $|\mathbf{u}| = U$ on the free streamlines, where $\mathbf{u}$ is fluid velocity, $\mathbf{n}$ the unit normal to the fibre, and U the flow speed at infinity. We take the simplest version of FST, which has an infinite wake and fluid pressure equal to wake pressure at the free streamlines. We set the far-field pressure p_∞ to zero. The formulation of ref. 17 is convenient, relating $\mathbf{u}$ to the body shape given as $\theta(s)$, the tangent angle as a function of the signed arc length s along the fibre.

Given $\mathbf{u}$, the pressure loading is given by the Bernoulli equation: $[p] = p_{\text{fibre}} - p_{\text{wake}} = p_{\text{fibre}} - p_\infty = \rho(U^2 - |\mathbf{u}_{\text{fibre}}|^2)/2$. Here p_{wake} is the far-field pressure, or zero, and hence the pressure jump across the fibre is p_{fibre}. In real flows, p_{wake} is nearly constant but significantly less than zero near the body, rising gradually to zero downstream. For this reason, the infinite-wake model must be modified to accurately represent the pressure distribution and drag on the body. This has usually been achieved with a more complicated wake structure which takes p_{wake} as an input parameter, generally determined by empirical considerations[18]. We retain the infinite-wake model with $p_{\text{wake}} = 0$, but instead apply a uniform multiplicative increase to the free-stream velocity in the model over that in the corresponding experiment. Through Bernoulli's equation, $[p]$ is then increased in a way similar to that achieved with a non-zero p_{wake}. This technique has produced good empirical results for wake models[19].

The pressure load is balanced by the fibre's tensile and bending forces:

$$-(T\mathbf{s})' + (E\kappa'\mathbf{n})' = fp_{\text{fibre}}\mathbf{n} \qquad (2)$$

with T the axial tension, $\kappa = \theta'$ the fibre curvature, and $\mathbf{s}$ its unit tangent vector. The superscript $'$ denotes differentiation with respect to arc length. Equation (2) is supplemented by 'free-end' boundary conditions: $T = \kappa = \kappa' = 0$ at fibre ends, $s = \pm L/2$. The fibre is fixed and clamped at its midpoint (that is, $\theta(0) = 0$).

Making the beam/FST system non-dimensional simplifies equation (2) to a nonlinear scalar equation for beam curvature:

$$\kappa'' + \frac{1}{2}\kappa^3 = \eta^2 p_{\text{fibre}} \qquad (3)$$

(A similar expression involving the curvature arises, for example, in studying the deformations of an inextensible elastic beam in a very viscous fluid[20].) This closes the model, with the non-dimensional speed η its only parameter. The beam/FST system is solved numerically (S.A., M.S. and J.Z., manuscript in preparation).

A solution is found for each value of η, giving fluid velocity and pressure fields, fibre shape, and free streamline shapes. Figure 2c
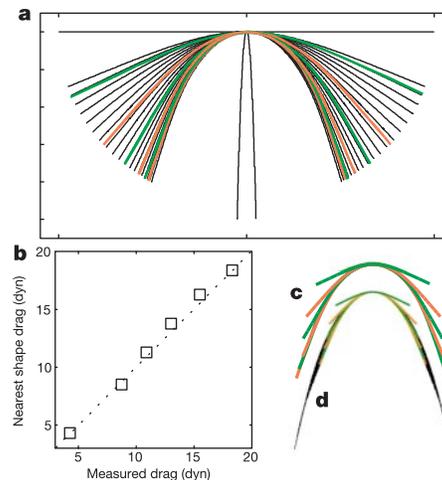

Figure 3 Comparison of six experimental fibre shapes with model shapes. **a,** Shapes from the experiment (green and orange lines) superimposed on a manifold of numerical solutions (black lines). The numerical solutions range from $\eta = 5.5$ to 33, in increments of 10%. The flat plate ($\eta = 0$) and a very bent solution ($\eta = 30{,}000$) are shown for comparison. **b,** Comparison of measured drag on experimental fibres in **a** with computed drag of nearest numerical solutions, determined by matching tip curvature. **c,d,** Transition to self-similarity in experimental (**c**) and numerical solutions (**d**) (not shown at the same scale). The six fibres, and their nearest numerical solutions, are dilated by $\eta^{2/3}$ and superimposed. The black fibres are numerical solutions at higher η, and show the subsequent convergence to a universal shape, as predicted by the model.
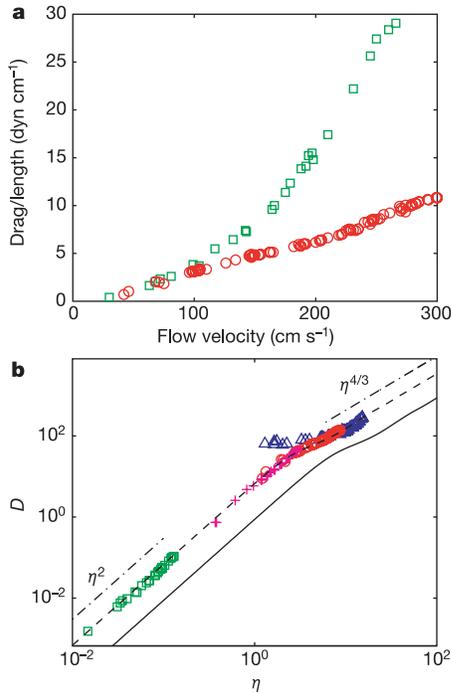
Figure 4 Comparison of drag data from experiment and model. **a**, Drag per unit fibre length versus flow velocity for a flexible fibre ($L = 3.3$ cm; red circles) and a rigid fibre ($L = 2.0$ cm; green squares). **b**, Log–log plot of drag data in **a**, non-dimensionalized as $D = C_D \eta^2$; also shown are data for two fibres with the same rigidity as the flexible fibre in **a** but different lengths (pink plus signs, $L = 1.8$ cm; blue triangles, $L = 5.2$ cm). The solid line is the values of D in the model (well-fitted by power laws η^2 for $\eta \ll 1$ and $\eta^{4/3}$ for $\eta \gg 1$, as shown by dash-dotted lines). The short-dashed line is the solid line shifted by a factor of 2.8 in η, to correspond with the shift in the shape comparison. This shift compensates for the 'back pressure' in the wake, as explained in the text.

shows a detailed solution, and Fig. 3a shows computed fibre shapes for η small to large. For $\eta \ll 1$, the fibre is nearly straight, but as η becomes O(1) there is a sharp transition to bending. The most notable property of the transition is an emerging self-similarity in fibre shape. For $\eta \gg 1$, large curvature becomes confined to an ever-smaller region near the tip as η increases. The length of this 'tip region' is proportional to the bending length, $L_0 = L\eta^{-2/3}$. This sets the scale for self-similarity: when dilated by $\eta^{2/3}$ the shapes overlap a universal, quasi-parabolic form (Fig. 3d). The transition is also captured in the computed dimensionless drag D (Fig. 4b). For $\eta \ll 1$ the model's drag scales quadratically, as does the experimental data; for $\eta \approx$ O(1), the model's drag undergoes a transition to a much slower growth, scaling as $\eta^{4/3}$ for $\eta \gg 1$.

Self-similarity of shape gives an interpretation for the $\eta^{4/3}$ drag-scaling. Rescaling arc length as $S = s\eta^{2/3}$, curvature as $\eta^{2/3}K(s\eta^{2/3}) = \kappa(s)$, and pressure as $P(s\eta^{2/3}) = p(s)$, equation (3) becomes $K^3/2 + K'' = P$, with η appearing only in the boundary conditions: $K = K' = 0$ at $S = \pm\eta^{2/3}/2$. As $\eta \to \infty$, K and P tend to the curvature and pressure of the universal shape. The drag is given by

$$D = \eta^2 \int_{\text{fibre}} [p]\, dy = \eta^{4/3} \int_{-\eta^{2/3}/2}^{+\eta^{2/3}/2} \left(\frac{1}{2}K^3 + K''\right) \frac{dY}{dS}\, dS \qquad (4)$$

where $Y = y\eta^{2/3}$. As $\eta \to \infty$, the integral converges to its value for the universal shape, and hence the drag scales as the prefactor $\eta^{4/3}$.

Figure 3a compares computed to experimental shapes for the full range of flow speeds. Aligning the midpoints, the relative displacement from the midpoint between the experimental shape and the nearest computed shape is less than five per cent over the entire

length. Figure 3c indicates the emergence of self-similarity in the experimental shapes, as in the computed shapes, though the upper limit on the soap-film flow speed impedes a thorough comparison for large η. In Fig. 3b the measured drag for the fibres is compared to that of their nearest computed solutions, demonstrating that the similar shapes in theory and experiment also give similar drags. We interpret this to mean that the model captures the nature of the pressure jump distribution across the fibre.

Through this comparison, we obtain a quantitative estimate for the multiplicative increase of η needed for the model to account for the wake pressure and its effect on the drag. The values of η for the corresponding theoretical and experimental fibre shapes of Fig. 3a differ by an almost uniform factor of 2.8. In Fig. 4b, the model and experiment show very similar drag scaling and transition when the theoretical curve is shifted leftward in η to adjust for this factor.

Fluid pressure and elastic bending forces seem sufficient to describe the drag reduction observed in our experiment. Though negligible for our flow speeds, skin friction may become important in much faster flows, where the fibre would be more swept-back, like a flat plate aligned with the flow. As implied earlier, the viscous drag on the fibre would then scale as $U^{3/2}$, eventually dominating the $U^{4/3}$ form drag.

A final comment concerns the relation of bending length to drag. Two-dimensional form drag usually scales as $\rho U^2 W$, where W is profile width. In our case, the parabolic form of the universal shape implies that W decreases as $\eta^{-1/3}$. Hence one would expect $D \sim \eta^{5/3}$. Instead we find that the drag is induced on the bending length $L_0 \sim \eta^{-2/3}$, giving the more slowly growing form $D \sim \eta^{4/3}$. In essence, the tip region creates a parabolic wake in which the rest of the body sits, contributing little to the drag. □

1. Batchelor, G. K. *An Introduction to Fluid Dynamics* (Cambridge Univ. Press, Cambridge, 1967).
2. Vogel, S. Drag and reconfiguration of broad leaves in high winds. *J. Exp. Bot.* **40,** 941–948 (1989).
3. Denny, M. Extreme drag forces and the survival of wind-swept and water-swept organisms. *J. Exp. Biol.* **194,** 97–115 (1994).
4. Koehl, M. How do benthic organisms withstand moving water? *Am. Zool.* **24,** 57–70 (1984).
5. Vogel, S. *Life in Moving Fluids* (Princeton Univ. Press, Princeton, 1994).
6. Couder, Y., Chomaz, J. M. & Rabaud, M. On the hydrodynamics of soap films. *Physica D* **37,** 384–405 (1989).
7. Gharib, M. & Derango, P. A liquid-film (soap film) tunnel to study two-dimensional laminar and turbulent shear flows. *Physica D* **37,** 406–416 (1989).
8. Goldburg, W. I., Rutgers, M. A. & Wu, X.-L. Experiments on turbulence in soap films. *Physica A* **239,** 340–349 (1997).
9. Rutgers, M. A., Wu, X.-L. & Daniel, W. B. Conducting fluid dynamics experiments with vertically falling soap films. *Rev. Sci. Instrum.* **72,** 3025–3037 (2001).
10. Zhang, J., Childress, S., Libchaber, A. & Shelley, M. Flexible filaments in a flowing soap film as a model for one-dimensional flags in a two-dimensional wind. *Nature* **408,** 835–839 (2000).
11. Segel, L. *Mathematics Applied to Continuum Mechanics* (MacMillan, New York, 1977).
12. Birkhoff, G. & Zarantonello, E. H. *Jets, Wakes, and Cavities* (Academic, New York, 1957).
13. Helmholtz, H. Uber discontinuierliche Flussigkeitsbewegungen. *Monatsber. Berlin Akad.* 215–268 (1868); reprinted in *Phil. Mag.* **36,** 337–346 (1868).
14. Dugan, J. P. A free-streamline model of the two-dimensional sail. *J. Fluid Mech.* **42,** 433–446 (1970).
15. Rivera, M., Vorobieff, P. & Ecke, R. E. Turbulence in flowing soap films: velocity, vorticity, and thickness fields. *Phys. Rev. Lett.* **81,** 1417–1420 (1998).
16. Rivera, M. & Wu, X.-L. External dissipation in driven two-dimensional turbulence. *Phys. Rev. Lett.* **85,** 976–979 (2000).
17. Hureau, J., Brunon, E. & Legallais, P. Ideal free streamline flow over a curved obstacle. *J. Comput. Appl. Math.* **72,** 193–214 (1996).
18. Wu, T. Y. Cavity and wake flows. *Annu. Rev. Fluid Mech.* **4,** 243–284 (1972).
19. Smith, F. T. Laminar flow of an incompressible fluid past a bluff body: the separation, reattachment, eddy properties and drag. *J. Fluid Mech.* **92,** 171–205 (1979).
20. Goldstein, R. E. & Langer, S. A. Nonlinear dynamics of stiff polymers. *Phys. Rev. Lett.* **75,** 1094–1097 (1995).

Correspondence and requests for materials should be addressed to M.S. (e-mail: shelley@cims.nyu.edu).